ACSNANO

www.acsnano.org

ARTICLE

Simultaneous Observation of Carrier-Specific Redistribution and Coherent Lattice Dynamics in 2H-$MoTe_2$ with Femtosecond Core-Level Spectroscopy

Andrew R. Attar,[▲] Hung-Tzu Chang,[▲] Alexander Britz, Xiang Zhang, Ming-Fu Lin, Aravind Krishnamoorthy, Thomas Linker, David Fritz, Daniel M. Neumark, Rajiv K. Kalia, Aiichiro Nakano, Pulickel Ajayan, Priya Vashishta, Uwe Bergmann,* and Stephen R. Leone*

Cite This: *ACS Nano* 2020, 14, 15829−15840

Read Online

ACCESS | Metrics & More | Article Recommendations | Supporting Information

ABSTRACT: We employ few-femtosecond extreme ultraviolet (XUV) transient absorption spectroscopy to reveal simultaneously the intra- and interband carrier relaxation and the light-induced structural dynamics in nanoscale thin films of layered 2H-$MoTe_2$ semiconductor. By interrogating the valence electronic structure via localized Te 4*d* (39−46 eV) and Mo 4*p* (35−38 eV) core levels, the relaxation of the photoexcited hole distribution is directly observed in real time. We obtain hole thermalization and cooling times of 15 ± 5 fs and 380 ± 90 fs, respectively, and an electron−hole recombination time of 1.5 ± 0.1 ps. Furthermore, excitations of coherent out-of-plane A_{1g} (5.1 THz) and in-plane E_{1g} (3.7 THz) lattice vibrations are visualized through oscillations in the XUV absorption spectra. By comparison to Bethe−Salpeter equation simulations, the spectral changes are mapped to real-space excited-state displacements of the lattice along the dominant A_{1g} coordinate. By directly and simultaneously probing the excited carrier distribution dynamics and accompanying femtosecond lattice displacement in 2H-$MoTe_2$ within a single experiment, our work provides a benchmark for understanding the interplay between electronic and structural dynamics in photoexcited nanomaterials.

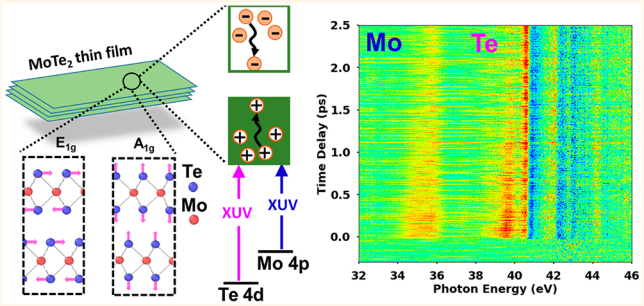

KEYWORDS: *transition metal dichalcogenide, $MoTe_2$, carrier thermalization, carrier-phonon scattering, coherent lattice vibration, extreme ultraviolet pump−probe spectroscopy*

The compound $MoTe_2$ is a member of the emerging class of two-dimensional layered transition metal dichalcogenide (TMDC) materials with atomically thin layers separated by weakly bound van der Waals interactions.[1−3] While $MoTe_2$ is stable in two structural phases at room temperature, including the semiconducting hexagonal (2H) and semimetallic monoclinic (1T′) phases, the more thermodynamically stable 2H-phase $MoTe_2$ has attracted significant interest due to its band gap of 0.9 eV in bulk and 1.1 eV in the monolayer, similar to that of Si (1.1 eV).[4] Recent investigations have shown the potential for integrating both monolayer and multilayer TMDC semiconductors into devices, including transistors,[5,6] photonic logic gates,[7] photodetectors,[8] and nonvolatile memory cells.[9] While the typical device application involves stacking different subcomponent thin-film materials into heterostructures to extend functionality,[7,9,10] the overall performance of TMDC-based devices can be dominated by the individual subcomponent's carrier dynamics.[11] For devices involving multilayer thin-films of 2H-$MoTe_2$, the carrier transport properties within the $MoTe_2$ subcomponent can dictate their functionality.[7,12] In addition to the carrier dynamics, there is a growing interest in the light-induced structural responses of TMDC's including $MoTe_2$ and

Received: August 19, 2020
Accepted: October 14, 2020
Published: October 21, 2020

https://dx.doi.org/10.1021/acsnano.0c06988
ACS Nano 2020, 14, 15829−15840

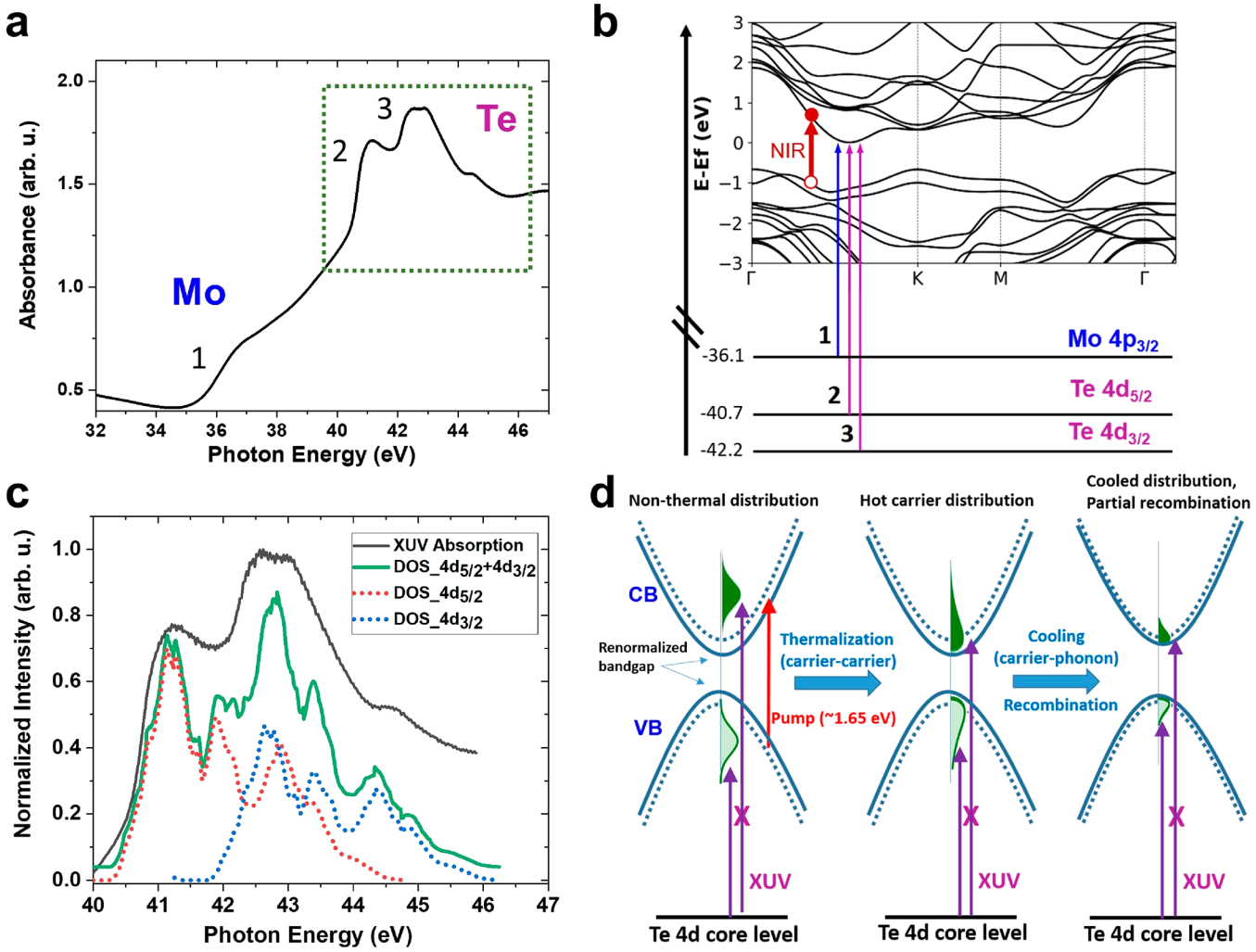

Figure 1. (a) Static XUV absorption spectrum of 2H-$MoTe_2$ with Mo $4p_{3/2}$ → CB and Te $4d_{5/2,3/2}$ → CB absorption edges labeled 1−3. The Mo $4p_{1/2}$ → CB edge is too weak to observe and is omitted. (b) Band structure of 2H-$MoTe_2$ along the Γ−K−M−Γ path. The corresponding core-level transitions for the three absorption edges labeled in (a) are shown by vertical blue and purple arrows and labeled 1−3 accordingly. Note that the arrows only show the *onset* of the core-level absorption edge for the case of the material without NIR−vis excitation. As the XUV energy is increased above each onset, carriers are promoted to higher energies in the CB at different positions throughout k-space. One representative VB → CB transition induced by the NIR−vis pump pulse (of the range of transitions possible from the broad bandwidth pump) is shown as a red arrow. (c) An expanded plot of the normalized XUV absorption spectrum in the Te window (black line). The red-dotted and the blue-dotted lines are plots of the calculated normalized CB DOS relative to the Te $4d_{5/2}$ core level (labeled DOS_$4d_{5/2}$) and $4d_{3/2}$ core level (labeled DOS_$4d_{3/2}$), respectively. The difference in the relative amplitudes of DOS_$4d_{5/2}$ and DOS_$4d_{3/2}$ is described in the main text. The sum of DOS_$4d_{5/2}$ and DOS_$4d_{3/2}$ is plotted (green solid line). (d) Model of the XUV transient absorption probing scheme for 2H-$MoTe_2$. The VB and CB are shown as parabolic bands. The solid (dashed) parabolas represent the bands with (without) band gap renormalization. The photoexcited holes and electrons are represented by the shaded light-green and dark-green areas, respectively. Representative XUV transitions from the Te 4*d* core levels are shown with and without an X to represent a decrease or increase in absorption relative to the static spectrum, respectively, due to state-filling.

WTe_2, especially for applications in optically controlled phase transitions.[13−15]

Recent studies have therefore aimed at characterizing the carrier relaxation and associated structural dynamics of few-layer and bulk 2H-$MoTe_2$.[14,16−18] Although the understanding of carrier-specific dynamics of holes and electrons is critical for designing ambipolar semiconductor devices,[12,19,20] separating the different contributions of the charge carriers by traditional time-resolved optical/IR and THz spectroscopies is challenging due to overlapping spectral features. This is exemplified by the studies of 2H-$MoTe_2$ by Li et al.[16] and Chi et al.,[17] where THz and optical experiments were used to measure the carrier lifetime, but without carrier specificity and without sensitivity to hot carrier intraband dynamics.

As a possible solution to these challenges, recent investigations have shown the potential of using ultrafast core-level spectroscopy such as XUV transient absorption to disentangle the intraband hole and electron dynamics in semiconductors.[21−25] In XUV transient absorption experiments, an optical pump pulse excites carriers across the band gap at time zero, and, at a series of controlled time delays, the energy-dependent change in carrier population is probed by core-level transitions to the partially occupied valence band (VB) and conduction band (CB). In some cases, photoexcited holes and electrons can be separately and simultaneously

https://dx.doi.org/10.1021/acsnano.0c06988
ACS Nano 2020, 14, 15829−15840

attributed to changes in spectrally distinct transitions from atomic core levels to the transiently empty states in the VB (holes) and reduced absorption in the transiently filled CB (electrons). These phenomena are collectively referred to here as "state-filling." It is possible not only to distinguish the hole and electron distributions but also to gain energy-dependent dynamics of the specific hot carriers within the VB and CB.[22,26] The element-specificity inherent to core-level spectroscopy offers the additional capability to distinguish the individual subcomponent materials in heterostructures.[27,28] Finally, the sensitivity of core-level spectroscopy to bonding, bond distances, and symmetry provides simultaneous structural information on photoexcited materials.[29−34]

In the present study, we apply sub-5 fs XUV transient absorption spectroscopy on a 2H-$MoTe_2$ semiconductor thin film (~50 nm/70 layers) to probe the dynamics of intraband carrier-specific relaxation, interband electron−hole recombination, and excited-state coherent lattice displacement. We obtain element-specific information by simultaneously measuring the spectral range around the Te $N_{4,5}$ absorption edge (39−46 eV) and the Mo N_3 edge (35−38 eV), as a function of delay time after optical excitation. The XUV absorption captures the same total density of states information at both edges. This enables us to analyze the hole distribution dynamics in the VB, distinguishing between thermalization of the holes by carrier−carrier scattering, subsequent cooling by carrier-phonon scattering, and the much slower electron−hole recombination process. We also report on the observation of light-induced coherent lattice vibrations in the out-of-plane A_{1g} and the in-plane E_{1g} modes of 2H-$MoTe_2$, which are captured via high-frequency oscillations (THz) in the XUV spectra. By comparison to *ab initio* Bethe−Salpeter equation simulations of the core-level absorption spectrum with different 2H-$MoTe_2$ lattice geometries, the excited-state displacement of the lattice that drives the coherent motion is extracted. Using this approach, we are able to capture the real-space lattice displacement simultaneously with the carrier−carrier thermalization of the holes, cooling (hole-phonon), and electron−hole recombination, leading to a cohesive picture of carrier and structural dynamics in a layered semiconductor nanomaterial.

RESULTS AND DISCUSSION

Experimental Scheme and Static Absorption of 2H-$MoTe_2$. The experimental apparatus and methodology of the XUV transient absorption spectroscopy measurements performed here have been previously described[21] and a detailed description is provided in the Methods section and the Supporting Information. The experiment is performed on a thin-film (50 nm thick, i.e. 70 layers) polycrystalline sample of 2H-phase $MoTe_2$, which is synthesized by chemical vapor deposition (CVD) onto a Si_3N_4 susbtrate of 30 nm thickness and 3 × 3 mm^2 lateral size. The sample is characterized by Raman spectroscopy to confirm the 2H-phase structure (see Supporting Information for sample preparation and detailed characterization).[3] In the XUV transient absorption experiments, this sample is photoexcited by a sub-5 fs, visible-to-near-infrared (VIS-NIR) pump pulse spanning 1.2−2.2 eV with an average photon energy of 1.65 eV. The initial photoexcited carrier density is ~1×10^{20} cm^{-3} (i.e., ~7×10^{12} cm^{-2} in each layer, given the ~0.7 nm thickness per layer), which corresponds to a 0.1% excitation fraction of the total valence electrons (see Supporting Information for details). The photoexcited sample is then probed at a controlled time delay, τ, by the arrival of a broad-band (30−50 eV), sub-5 fs XUV pulse produced by high-harmonic generation. The transmitted XUV intensity through the sample is measured as a function of photon energy, I(E), by a spectrometer. The transient absorption signal, $\Delta OD(E, \tau) = OD_{pump\text{-}on}(E, \tau) - OD_{pump\text{-}off}(E)$, is determined by the difference between the XUV absorbance, or optical density (OD), of the photoexcited sample at time τ and the static XUV absorbance in the absence of pump excitation.

The broad-band XUV pulse allows for the simultaneous absorption measurement covering the Mo $N_{2,3}$ edges (~35−38 eV, referred to as the "Mo window") and the Te $N_{4,5}$ edges (39−46 eV, referred to as the "Te window"). The transmission of the broad-band XUV spectrum (Figure S1c) is referenced to the transmission of a blank Si_3N_4 substrate to obtain the static absorption spectrum of the thin-film 2H-$MoTe_2$ sample: i.e., absorbance $A = \log(I_{blank}/I_{sample})$, which is shown in Figure 1a. XUV transitions in the Mo and Te windows occur by promotion of Mo $4p_{3/2,1/2}$ and Te $4d_{5/2,3/2}$ core electrons to the CB, respectively. The onset of the transitions from each observed core level is labeled 1−3 in Figure 1a, and the corresponding transition is shown schematically in Figure 1b. Note that the arrows in Figure 1b only show the *onset* of each core-level absorption edge. As the XUV energy is increased above each onset, carriers are promoted from the corresponding core level to higher valleys in the CB at different k-space positions throughout the Brillouin zone. In the Mo window, the onset of transitions from the Mo $4p_{1/2}$ core level is too weak to observe in the static spectrum and is omitted from the analysis. The onset of Mo $4p_{3/2} \rightarrow$ CB absorption is measured at 36.1 eV and labeled edge 1. In the Te window, the onset of the Te $4d_{5/2} \rightarrow$ CB (edge 2) is measured at 40.7 eV and the onset of the Te $4d_{3/2} \rightarrow$ CB (edge 3) is at 42.2 eV. The 1.5 eV separation of edges 2 and 3 matches the Te $4d_{5/2,3/2}$ spin−orbit splitting in $MoTe_2$ confirmed by XPS spectra (Supporting Information Figure S3). When the VIS−NIR pulse excites the material, additional transitions become accessible from the core levels to the VB and transitions to the CB can be reduced due to state-filling, as discussed below.

Considering more closely the Te window (Figure 1c), the relatively sharp features allow for a detailed mapping of the CB density of states (DOS) from the Te 4*d* core levels. First, DOS calculations are performed, which are described and shown in detail in the Supporting Information, Figure S4. In Figure 1c, the calculated CB density of states (DOS) is plotted relative to the $4d_{5/2}$ core level (red dashed line, labeled DOS_$4d_{5/2}$) and to the $4d_{3/2}$ core level (blue dashed line, labeled DOS_$4d_{3/2}$). The relative amplitudes between DOS_$4d_{5/2}$ and DOS_$4d_{3/2}$ is set according to the expected degeneracies of the core-hole total angular momentum J states (J = 5/2 versus J = 3/2), which, to first approximation, predicts a 3:2 ratio for $4d_{5/2} \rightarrow$ CB versus $4d_{3/2} \rightarrow$ CB amplitudes. The resulting core-hole-mapped DOS (green solid line) is compared to the experimental XUV absorption spectrum (black solid line). The close agreement between the calculated CB DOS and the XUV absorption spectrum in Figure 1c demonstrates that the core hole of the Te $N_{4,5}$ absorption is well screened such that the core-level absorption spectrum can be regarded as a map of the CB unoccupied DOS in the valence shell.

Within this picture, the probing scheme for measuring the carrier dynamics following optical excitation can be understood by the model illustrated in Figure 1d. In the leftmost panel, above-band-gap photoexcitation produces a nonthermalized

https://dx.doi.org/10.1021/acsnano.0c06988
ACS Nano 2020, 14, 15829−15840

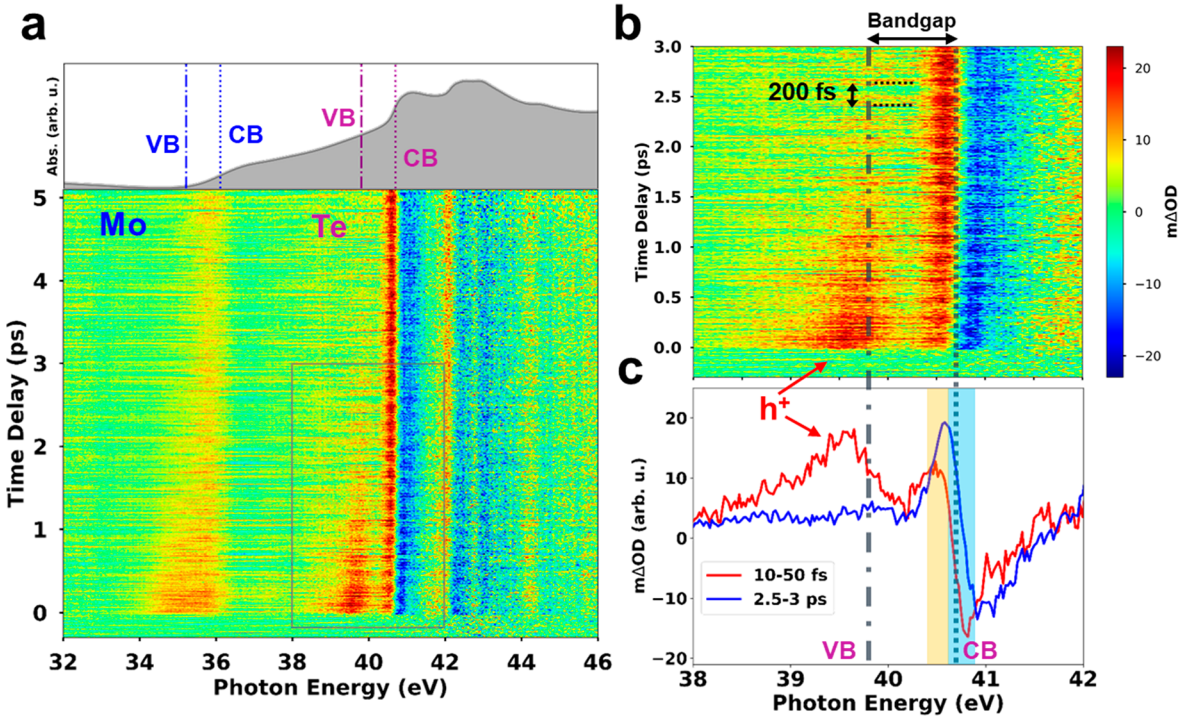

Figure 2. (a) XUV transient absorbance in a false-color plot versus time shown in the bottom panel and compared to the static absorbance spectrum in the top panel. The vertical dotted and dash-dotted lines in the upper panel are drawn at the energies corresponding to the CB minimum and VB maximum, respectively, from both the Mo $4p_{3/2}$ and Te $4d_{5/2}$ core levels. (b) Transient absorbance in a false color plot versus time, expanded from the gray box region in the lower panel of (a). The indicated 200 fs oscillations in the differential absorbance are discussed further in the final section of the paper. (c) Differential absorbance lineouts averaged over early time delays (10−50 fs) and long time delays (2.5−3 ps). Orange and blue shaded regions indicate the energy windows used for temporal lineouts in Figure 5.

distribution of carriers corresponding to a convolution of the excitation spectrum and the VB/CB DOS. The broad-bandwidth excitation in the present experiment produces carriers over a large range of momentum values in k-space. Moving from left to right in Figure 1d, the initial nonthermal carrier distribution is expected to undergo carrier−carrier thermalization, carrier−phonon cooling, and recombination in accordance with known carrier−carrier and carrier−phonon scattering processes in semiconductors.[35] These carrier dynamics lead to energy- and time-dependent changes in the unoccupied DOS within the VB and CB, as shown in the schematic. For example, the peak of the hot hole distribution is expected to shift upward toward the VB maximum due to both thermalization and cooling, which can occur on time scales of 10s to 100s fs.[35−38] The corresponding changes to the XUV absorption (ΔOD) due to state-filling effects[21−23,26] are schematically illustrated by vertical arrows from the representative Te 4*d* core level. In the following sections, the time-resolved ΔOD of the spectrally dispersed XUV probe is used to extract both the carrier distribution and population dynamics in 2H-$MoTe_2$, revealing the individual steps depicted in Figure 1d. Due to the sharper XUV absorption edge observed in the Te window as compared to the Mo window, we focus primarily on the Te N-edge to report on the carrier and structural dynamics in this work. However, as shown in the Supporting Information in Figure S6 and Figure S9, the Mo $4p_{3/2}$ core level can also be used to capture the hole population dynamics and the coherent phonon dynamics, respectively.

XUV Transient Absorption Following Broadband Photoexcitation. In Figure 2a, the change in the XUV absorbance, ΔOD (E, τ), following VIS−NIR excitation is plotted in a false-color map as a function of time delay and photon energy. Changes are observed in both the Mo and Te windows near 33−37 eV and 38−46 eV, respectively. The ground-state absorbance spectrum of 2H-$MoTe_2$ is shown here again in the upper panel of Figure 2a to emphasize where the major pump-induced absorption changes appear relative to the static spectrum. The dotted vertical lines in Figure 2a (upper panel) at 36.1 and 40.7 eV show the energies of the Mo $4p_{3/2}$ → CB minimum and the Te $4d_{5/2}$ → CB minimum, respectively. With a bulk band gap of 0.9 eV in 2H-$MoTe_2$, the dash-dotted vertical lines at 35.2 and 39.8 eV correspond to the derived VB maximum energy relative to the Mo $4p_{3/2}$ and Te $4d_{5/2}$ core levels, respectively. Clear ΔOD signals are observed near these energies in the photoexcited sample. We focus first on the Te window in the gray box region of Figure 2a (lower panel), which is blown up for clarity in Figure 2b. At energies above 42 eV within the Te window, the XUV absorption spectrum involves overlapping transitions from both the Te $4d_{5/2}$ and the Te $4d_{3/2}$ core levels, as shown in Figure 1c. Below 42 eV (i.e., 38−42 eV), however, the spectrum is characterized by resonant transitions involving only the Te $4d_{5/2}$ core level, which greatly facilitates the analyses and interpretation of experimental spectra in this region. Two ΔOD spectral lineouts in this energy window are shown in Figure 2c, averaged over short (10−50 fs) and long delay times (2.5−3 ps). Within this energy range (38−42 eV), the resonant transitions correspond to promotion of an electron primarily from the Te $4d_{5/2}$ core level into the unoccupied DOS of the VB and CB.

Two main features are observed in the differential spectra at early delay times (10−50 fs window): a positive peak

https://dx.doi.org/10.1021/acsnano.0c06988
ACS Nano 2020, 14, 15829−15840

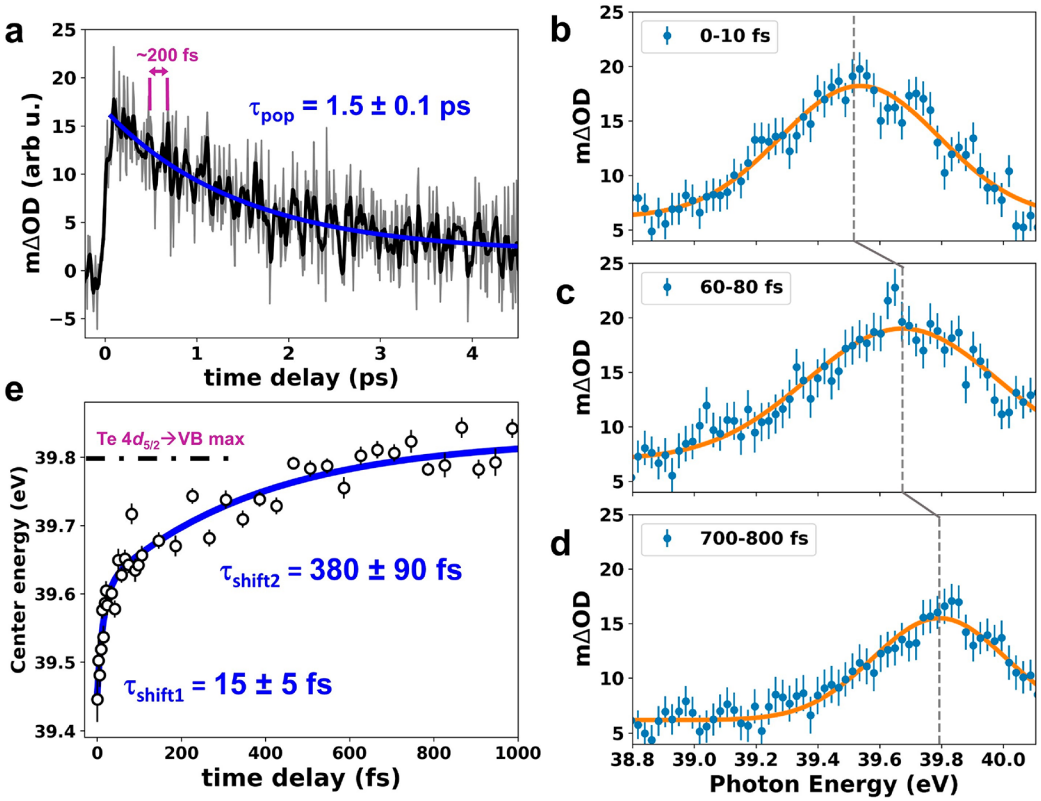

Figure 3. (a) Hole population dynamics measured as the integrated ΔOD amplitude at 39.7−39.9 eV versus time delay. The gray solid line is the experimental absorption data, and the black solid line is a rolling average over 7 delay points. A single exponential decay is fit to the data (blue solid line) with a time constant of 1.5 ± 0.1 ps. (b−d) Differential absorption of the Te $4d_{5/2}$ → VB hole signal at time delays of 0−10 fs, 60−80 fs, and 700−800 fs. The closed circles are the experimental absorption data, and the solid orange lines are Voigt fits. The gray dashed vertical lines show the center energy of the Voigt fit in each time slice. Blue arrows show the energy shift observed between time slices. Each differential absorption spectrum is an average over 10 time points within the designated time window. At each time point, 36 ΔOD spectra are averaged and the error bars are calculated as the standard error of the mean. The error for each time point is then propagated in the average of the 10 time points for each window and plotted with the data. (e) Hole distribution dynamics determined by extracting the center energy of the Te $4d_{5/2}$ → VB hole signal using a Voigt fit at each time delay. The open circles are the extracted center energies, and the error bars represent the standard error of the center energy fitting parameter in each Voigt fit. A biexponential decay function is fit (solid blue line) to the data with time constants of 15 ± 5 fs and 380 ± 90 fs.

appearing near 39.5 eV and a derivative-shaped feature centered at the onset of the ground-state $4d_{5/2}$ → CB absorption edge at 40.7 eV. The positive feature centered at 39.5 eV appears 0.3 eV below the derived $4d_{5/2}$ → VB maximum (shown as dash-dotted vertical line). This feature is therefore assigned to transitions from the $4d_{5/2}$ core level to "hot" holes in the VB produced by the above-band-gap photoexcitation (schematically represented by the left panel in Figure 1d). In the later time window (2.5−3 ps), the $4d_{5/2}$ → VB hole feature has disappeared and the derivative feature is characterized by a slight blue shift relative to the early delay times and a significant increase in absorption at energies between 40.6 and 40.9 eV. Several effects contribute to the derivative feature, including state-filling by the electrons in the CB and band gap renormalization (BGR), as schematically illustrated in Figure 1d.[21,23,30] These overlapping effects, which are discussed in detail below, make the electron state-filling signal less straightforward as compared to the hole signal. In the following, we therefore concentrate first on extracting the hole distribution and population dynamics from the temporal evolution of the $4d_{5/2}$ → VB signal centered near 39.5 eV.

Hole Distribution and Population Dynamics in the Valence Band. In order to track the detailed dynamics of both the population and distribution of the holes in the VB, we measure the time-dependent amplitude (population) and the central energy (distribution) of the $4d_{5/2}$ → VB peak. In Figure 3a, the hole population measured via the integrated $4d_{5/2}$ → VB absorption amplitude near the VB maximum (39.7−39.9 eV) is plotted as a function of delay time. The population decay is fit to a single exponential with a time constant of τ_{pop} = 1.5 ± 0.1 ps, which is assigned to electron−hole recombination. The fit to an exponential decay is chosen to provide a direct comparison to recent Mid-IR and THz transient absorption measurements of the carrier lifetime in 2H-phase $MoTe_2$.[16,17] In the THz study,[16] the carrier lifetime is found to be dominated by a phonon-mediated trapping/recombination mechanism, accelerated by Auger scattering, which can be reduced to a single exponential decay constant of ∼2 ps. This is consistent with our result of τ_{pop} = 1.5 ± 0.1 ps, but here we can explicitly assign this time constant to electron−hole recombination with minimal contributions from long-lived carrier traps. Any long-lived trapped holes would still be visible in the XUV transient absorption spectrum, if present in sufficient densities,[22] but no evidence for these long-lived hole states is evident after a few picoseconds (see Supporting Information Figure S5). The population dynamics of the holes can also be independently extracted from the Mo edge by measuring the decay of the integrated Mo $4p_{3/2}$ → VB

https://dx.doi.org/10.1021/acsnano.0c06988
ACS Nano 2020, 14, 15829−15840

signal at 35.1−35.3 eV (Supporting Information Figure S6). A time constant of τ_{pop} = 1.4 ± 0.1 ps is extracted, which matches the measurement in the Te window within the error bars.

Turning now to the distribution dynamics of the holes within the VB, we first examine more closely the Te $4d_{5/2}$ → VB hole feature at three representative time slices of 0−10 fs, 60−80 fs, and 700−800 fs plotted in Figure 3b−d. The spectrum of the hole feature is interpreted in accordance with the one-particle picture to directly record the hole energy distribution within the VB. In each time slice, the Te $4d_{5/2}$ → VB peak is fit by a Voigt function to take into account the photoexcitation bandwidth, which produces a broad hole distribution approximated by a Gaussian function, and the convolved Lorentzian core-hole lifetime broadening. In the first time slice (0−10 fs), the $4d_{5/2}$ → VB signal is centered at 39.5 eV, which is 0.3 eV below the $4d_{5/2}$ → VB maximum. This peak is assigned to $4d_{5/2}$ core transitions to the nascent, nonthermal hole distribution in the VB, which is represented by the schematic illustration in the left panel of Figure 1d. In the 60−80 fs time slice in Figure 3c, the $4d_{5/2}$ → VB hole feature has blue-shifted from 39.5 to 39.65 eV. This shift of the holes to higher energies is interpreted as a combination of carrier−carrier (i.e., hole−hole or hole−electron) thermalization and partial hole-phonon cooling of the nascent hole distribution, which correlates to the middle and right panels of the schematic model in Figure 1d. Note that while thermalization by carrier−carrier scattering does not lead to a change in the total energy of the carrier distribution, the *peak* of the hole distribution still shifts toward the VB maximum by thermalization to a Fermi−Dirac distribution (see Supporting Information, Figure S7). A slight asymmetry is observed in the feature at 60−80 fs (Figure 3c), which could be an indication of the formation of a Fermi−Dirac distribution, but the peak is still fit well by a broad Voigt distribution. In the 700−800 fs time slice in Figure 3d, the hole feature is blue-shifted further to the VB maximum at 39.8 eV and the overall amplitude of the peak is decreased. This 700−800 fs time slice is interpreted in accordance with the rightmost panel of Figure 1d. The blue shift toward the VB maximum represents near-complete cooling of the holes, and the decay of the integrated area of the signal is caused by partial loss of hole population due to electron−hole recombination.

To map the full evolution of the hole distribution, the Voigt fitting procedure of the $4d_{5/2}$ → VB peak is repeated for each time delay within the lifetime of the hole population and the extracted Voigt center energies are plotted as a function of delay time in Figure 3e. Although the hole distribution can also be fit by a Fermi−Dirac distribution at intermediate delay times to monitor the hole cooling process,[26] one can only define a carrier temperature in terms of a Fermi−Dirac distribution after thermalization has occurred. Since one of our primary goals is to distinguish the thermalization and cooling time scales of the holes, the Voigt fitting procedure used here allows us to trace the entire hole relaxation process using a single time-dependent parameter. The observed hole energy distribution dynamics in Figure 3e can be described by a biexponential energy shift with a fast time constant (τ_{shift1} = 15 ± 5 fs) and a slower component (τ_{shift2} = 380 ± 90 fs). A monoexponential fit was also attempted, but did not result in a good agreement with our data (see Supporting Information Figure S7). The initial energy redistribution time scale (τ_{shift1} = 15 ± 5 fs) from the biexponential fit is very similar to the <20 fs time constant measured by Nie et al. in MoS_2 for carrier−carrier scattering using optical transient absorption spectroscopy.[37] In the experiment by Nie et al., the hole and electron dynamics are not distinguished and the optical spectrum is blind to the distinct energy distributions of the carriers. However, the <20 fs time constant is assigned in that work to thermalization by carrier−carrier scattering, which is supported by *ab initio* calculations.

In our experiment, the τ_{shift1} = 15 ± 5 fs measured in the peak of the carrier-specific hole distribution energy in 2H-$MoTe_2$ is assigned to a similar thermalization step via hole carrier−carrier scattering, as schematically represented in Figure 1d (left to middle panels). This assignment is consistent with a recent calculation of carrier−carrier scattering in monolayer 2H-$MoTe_2$ at similar carrier densities (per layer), which predicts a thermalization time of sub-20 fs.[39] This is also consistent with carrier−carrier thermalization time scales measured in other semiconductors including lead iodide perovskite[36] and other layered materials including graphite.[40] Additionally, intra- or intervalley scattering processes involving carrier−phonon interactions may also contribute. An intervalley scattering time of 70 fs was measured, for example, in another TMDC semiconductor, WSe_2, via ultrafast angle-resolved photoemission spectroscopy at similar excitation fluences.[41] However, the hole distribution in 2H-$MoTe_2$ measured here does not reach the global maximum of the VB, which is localized at the Γ point (Figure 1b), until after the slower time constant of t_{shift2} = 380 ± 90 fs. The hole distribution energy then remains constant near the VB maximum over the remaining hole population lifetime of τ_{pop} = 1.5 ± 0.1 ps. The slower hole redistribution time of t_{shift2} = 380 ± 90 fs is therefore assigned to hole-phonon cooling via intra- or intervalley scattering in the VB to the Γ point, allowing the carriers and lattice to come into thermal equilibrium before electron−hole recombination takes place.

Spectral Decomposition of Conduction Band Transients. We now discuss the derivative feature in the transient spectra near the onset of the $4d_{5/2}$ → CB absorption (~40.7 eV). Several effects contribute to this feature including band gap renormalization (BGR) and state-filling by the electrons in the CB (illustrated in Figure 1d), excited-state broadening, and local modifications to the structural environment due to phonon excitations.[21,23,30] In Figure 4, the Te window ΔOD spectrum in the time slice immediately following photoexcitation (0−10 fs) is plotted along with a manual decomposition of the broadening, BGR, and state-filling contributions in this energy window (further details in Supporting Information). The decomposition is performed using a similar procedure to that used by Zürch et al. on Germanium.[21]

The BGR and broadening contributions are calculated starting from the measured static XUV absorption spectrum by applying a linear energy shift and convolving the spectrum with a Gaussian filter, respectively. The state-filling effects are modeled by Voigt functions with a positive (negative) ΔOD sign for holes (electrons) and by taking into account the known spin−orbit splitting of the Te $4d_{5/2}$ and Te $4d_{3/2}$ core levels. The unknown parameters of the shift, broadening, and state-filling contributions are manually adjusted to find a qualitative match with the spectrum in Figure 4. The resulting decomposition shows that the Te $4d_{5/2}$ → VB hole signal is clearly isolated from the other transient effects, which makes the interpretation of this feature straightforward (as exploited in the previous section). The situation is less straightforward

https://dx.doi.org/10.1021/acsnano.0c06988
ACS Nano 2020, 14, 15829−15840

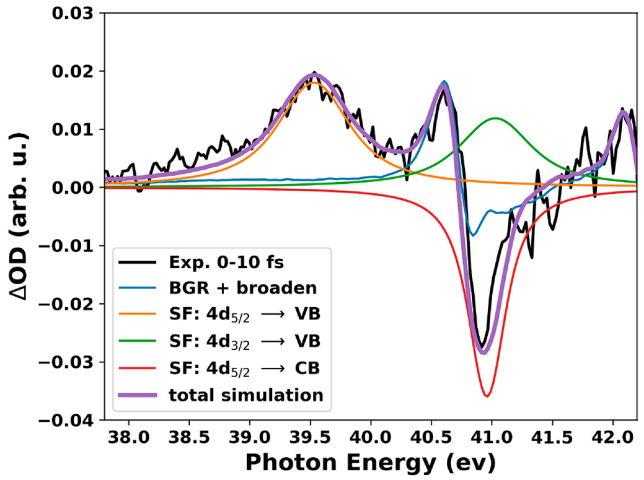

Figure 4. Solid black line is the experimental transient absorption data at a time delay of 0−10 fs. The colored solid lines are the manually decomposed contributions from the state-filling (SF), broadening, and bandgap renormalization (BGR), which are determined by the procedure described in the main text with further details in the Supporting Information. The total sum of the decomposed contributions is shown as the solid purple line.

for the electron signal (state-filling: Te $4d_{5/2}$ → CB), which overlaps with the Te $4d_{3/2}$ → VB hole signal and the BGR and broadening contributions of the Te $4d_{5/2}$ → CB edge. Using spectral decomposition to extract the electron state-filling signal is possible at short delays when the signal is strong, as shown in Figure 4, but as the carriers recombine at later times, the decomposition becomes less reliable. In the next section, therefore, we analyze the time-dependent ΔOD observed near the Te $4d_{5/2}$ → CB edge (40.65 to 40.9 eV) in terms of both the decay in this electron state-filling contribution and the overlapping evolution of the broadening and BGR related to recombination.

Electron Population Dynamics and Recombination-Induced Lattice Heating. In Figure 5a, the integrated differential absorption amplitude at energies near the onset of the $4d_{5/2}$ → CB edge (40.65 to 40.9 eV, marked as blue shaded region in Figure 2c) is plotted as a function of delay time. The initial decrease in absorption at t = 0 is followed by a slow increase, leading to an overall positive differential absorption after ∼2 ps. The slowly evolving increase is fit to a single exponential growth, and a time constant of 1.6 ± 0.1 ps is extracted. This time constant matches well with the decay of the hole signal shown in Figure 3a. Two overlapping effects can contribute to the increase in absorption between 40.6 to 40.9 eV, both of which are caused by electron−hole recombination. The first is the electron kinetics in the CB. As illustrated schematically in Figure 1d and demonstrated by the spectral decomposition in Figure 4, the initial state-filling effect in the CB leads to a decrease in absorption at these energies immediately following photoexcitation. When electron−hole recombination occurs, this causes the reopening of these states with a corresponding increase in the $4d_{5/2}$ → CB absorption. Second, nonradiative electron−hole recombination leads to a concomitant increase in the lattice thermal energy. Structural modifications caused by lattice heat can lead to a corresponding increase in the $4d_{5/2}$ core-level transitions at energies just below the CB minimum due to shifting and broadening effects.[23,42] This is evidenced by the increase in differential absorption at these photon energies in a continuously heated sample compared to the room temperature sample (details in Supporting Information Figure S5). Since both of these recombination-induced effects can lead to the observed increase in the XUV absorption at 40.65−40.9 eV, we assign this time-dependent increase as a signature of the electron population decay and corresponding nonradiative lattice heating.

Coherent Lattice Displacement Dynamics. Superimposed on the slowly varying ΔOD signal described in the previous section, high-frequency oscillations in ΔOD are evident near the derivative feature. In Figure 5b, the ΔOD at XUV energies where the largest-amplitude oscillations are observed (40.45−40.65 eV, marked as orange shaded region in Figure 2c) is plotted as a function of delay time. The inset in Figure 5b shows the high-frequency oscillations at 40.45−40.65 eV after subtraction of the slowly varying signal. In Figure 5c, the Fourier transform (FT) spectrum of the time-domain oscillations in the Figure 5b inset is plotted, showing the presence of two clear vibrational frequencies at 169 cm^{-1} (5.1 THz) and 122 cm^{-1} (3.7 THz). These frequencies match closely to the A_{1g} out-of-plane and E_{1g} in-plane optical phonon modes of 2H-$MoTe_2$, respectively, as observed by Raman scattering[43] (Supporting Information Figure S2). The phonon motions associated with these modes are shown schematically in Figure 5c.

From the FT spectrum in Figure 5c, the amplitude of the coherent oscillations in the XUV spectra is dominated by the A_{1g} mode, which is similar to the observation of coherent phonons through transient optical transmission measurements in MoS_2 and WSe_2.[44,45] We note that the E^1_{2g} mode is not observed in the FT spectrum at the characteristic frequency seen in the Raman spectrum (232 cm^{-1}); however, there may be evidence for a small contribution by this mode, which we describe in the Supporting Information (Figure S10). While the largest-amplitude oscillations are observed near the Te $4d_{5/2}$ → CB edge (40.45−40.65 eV), oscillations at the dominant A_{1g} frequency are also seen in other spectral regions, including near the hole signal in the Te window and near the Mo edge (see Supporting Information Figure S11). Focusing on the 40.45−40.65 eV region, the oscillating signal plotted in the inset of Figure 5b can be fit (blue line) using the following function:

$$\Delta\mathrm{OD}(t) = \alpha_1 \cos(2\pi\omega t_1 + \phi_1) + \alpha_2 \cos(2\pi\omega t_2 + \phi_2) \quad (1)$$

where α_n, ω_n, and ϕ_n correspond to the amplitude, frequency, and phase of the n^{th} vibrational component. The fitted frequencies are ω_1 = 5.08 ± 0.01 THz and ω_2 = 3.69 ± 0.02 THz, in agreement with what we observe in the FT spectrum in Figure 5c, and the fitted phases are φ_1= 0.95π ± 0.07π and φ_2 = 0.1π ± 0.2π.

There are two possible mechanisms for the observed coherent phonon generation when the optical pump pulse is resonant with the electronic excitations of the material. First, the electronic excitation can lead to a direct change in the charge density of the electronic excited state and drive the nuclei to the new minimum of the potential energy surface. This mechanism is referred to as "displacive excitation of coherent phonons" (DECP).[46] Second, the optical pump pulse can couple the ground-state electronic wave function to the potential energy surfaces of electronic excited states through resonant impulsive stimulated Raman scattering (ISRS),

https://dx.doi.org/10.1021/acsnano.0c06988
ACS Nano 2020, 14, 15829−15840

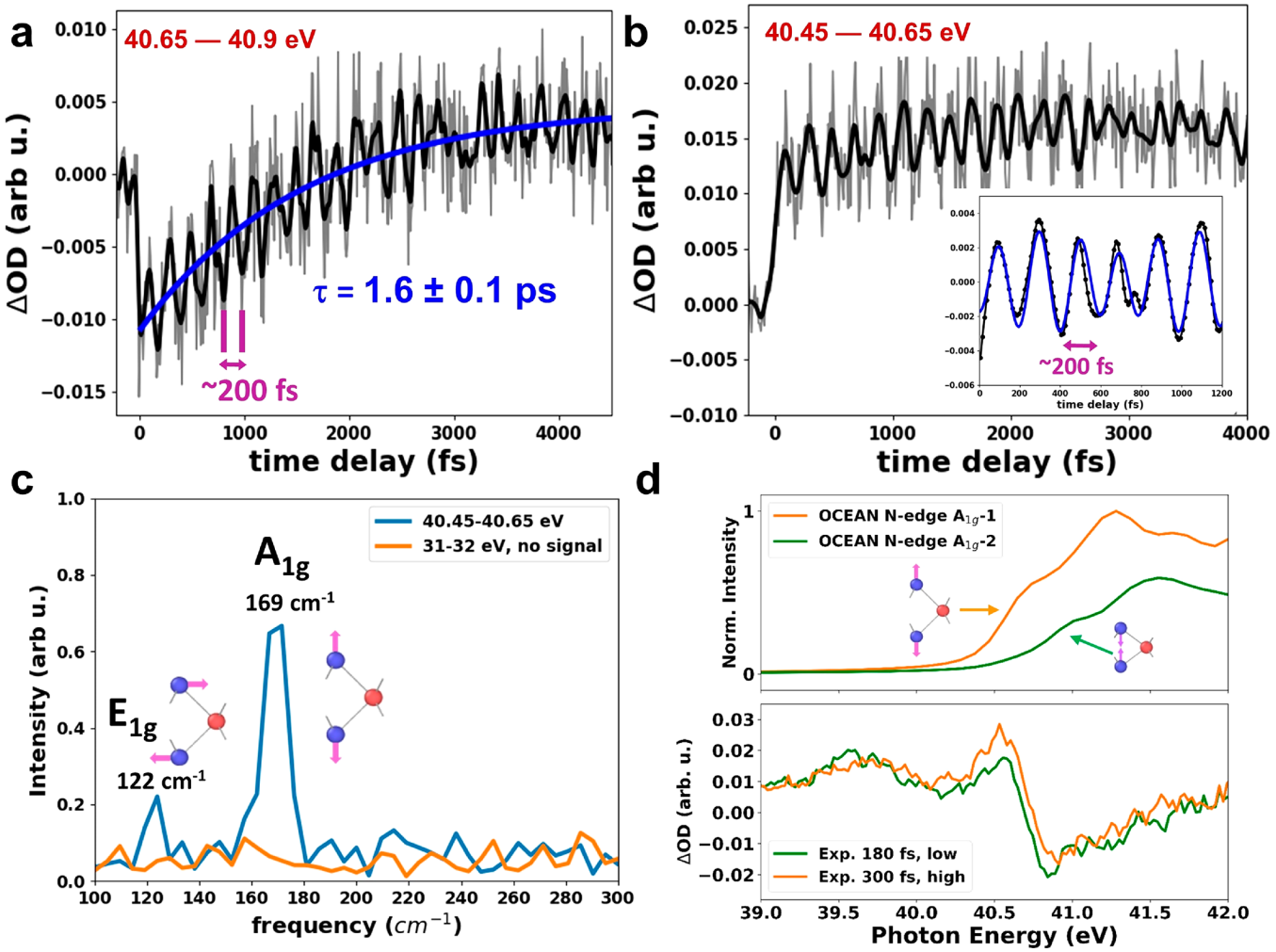

Figure 5. (a) Time evolution of the integrated ΔOD at photon energies just above the $4d_{5/2}$ → CB edge (40.65—40.9 eV). This energy range is indicated by the blue shaded region in Figure 2c. The gray line is the experimental data, and the black line is a 7-point rolling average over delay time. The blue line is a single exponential fit to the data with a time constant of 1.6 ± 0.1 ps. (b) Time evolution of the ΔOD just below the onset of the Te $4d_{5/2}$ → CB edge (40.45—40.65 eV). This energy range is indicated by the orange shaded region in Figure 2c. The gray solid line is the experimental absorption data, and the black line shows a 7-point rolling average (smoothed) over delay time. The inset shows a cosine fit to the smoothed data as described in the main text. (c) The Fourier transform (FT) spectrum of the time-dependent ΔOD signal in (b) is shown as a solid blue line, revealing peaks at 169 cm^{-1} (5.1 THz) and 122 cm^{-1} (3.7 THz). The orange line is the FT spectrum of the time-dependent ΔOD integrated over 31−32 eV (i.e., where no transient absorption signal is observed) to illustrate the noise floor. The inset shows a schematic of the displacive excitation mechanism, as described in the main text. (d) The upper panel shows the simulated displacement-induced change in the XUV spectrum calculated by OCEAN for each A_{1g} distortion direction. The bottom panel shows the experimental ΔOD data at time slices of 180 and 300 fs, respectively, demonstrating the uniform increase/decrease of the absorption near these energies at the two extremes of the coherent oscillation.

resulting in a force driving coherent vibrations of the lattice.[47] As mentioned by Trovatello et al.,[45] a consensus as to the dominant mechanism in the absorptive regime has not been established in the literature. Both mechanisms can produce displacive coherent phonons with cosine phases of 0 or π.[48,49] For this reason, the Raman scattering mechanism is also termed "transient stimulated Raman scattering" (TSRS) in the absorptive regime, to account for the possibility of inducing a displacive force by this mechanism.[49] However, while the DECP mechanism favors only coherent phonon excitations of totally symmetric modes (A_{1g}),[46,50] the Raman scattering mechanism allows excitation of all Raman-active modes. Therefore, the excitation of both A_{1g} and E_{1g} modes (Figure 5c) indicates that TSRS contributes to the coherent phonon excitation in 2H-$MoTe_2$. Regardless of the mechanism, the force induced by interaction with the ultrashort resonant excitation pulse in 2H-$MoTe_2$ is clearly displacive and not impulsive, as determined by the extracted phases ($\varphi_1 = 0.95\pi \pm 0.07\pi$ and $\varphi_2 = 0.1\pi \pm 0.2\pi$). With this information, our aim is to extract the real-space lattice displacement involved.

To understand the XUV ΔOD oscillations in terms of real-space lattice displacements, we first calculate distorted 2H-$MoTe_2$ structures along the dominant A_{1g} displacement coordinate. This is achieved by displacing each atom, i, with mass m_i located at r_i in the $MoTe_2$ unit cell by a distance Δr_i along the real part of the eigenvector, e, corresponding to the dominant A_{1g} vibration mode, $q = \Gamma$, computed as $\Delta r_i = \alpha/\sqrt{m_i}\,\mathrm{Re}[e\exp(q\cdot r_i)]$. The amplitude of the displacement, α, is chosen such that the maximum real-space displacement of any atom in the simulation cell is less than 0.3 Å. Next, Bethe−Salpeter equation calculations of the A_{1g}-distortion-dependent Te $4d$ → CB transitions are performed

https://dx.doi.org/10.1021/acsnano.0c06988
ACS Nano 2020, 14, 15829−15840

using the OCEAN (Obtaining Core-level Excitations using *ab initio* methods and the NIST BSE solver) software package.[51,52] The results are plotted in Figure 5d (upper panel). The calculations reveal that the XUV absorption amplitude at the $4d_{5/2} \rightarrow$ CB onset reaches a maximum when the Te atoms are moved outwardly in the direction away from the plane of Mo atoms. In the opposite direction, corresponding to the Te atoms moving inwardly toward the plane of Mo atoms, the XUV absorption amplitude decreases and slightly blue shifts near the $4d_{5/2} \rightarrow$ CB onset. This uniform decrease/increase over the $4d_{5/2} \rightarrow$ CB spectral region qualitatively matches the observed ΔOD oscillations in the experiment, as shown in the bottom panel of Figure 5d. From the phase of the A_{1g} oscillation (π) extracted from the experimental data in Figure 5b, the displacement at $t = 0$ begins with increasing absorption near the $4d_{5/2} \rightarrow$ CB onset. This shows that photoexcitation leads to a displacement along the A_{1g} mode in the outward direction. This ultrafast lattice expansion along the specific A_{1g} phonon mode in the excited state provides a key experimental benchmark for understanding how light-induced changes in electronic structure can drive nonthermal structural changes in layered materials.

CONCLUSIONS

In a single optical pump, XUV transient absorption probe experiment, we simultaneously uncover the detailed dynamics of intraband hole relaxation, electron−hole recombination, and excited-state coherent lattice displacement in 2H-$MoTe_2$. In contrast to optical transient absorption spectroscopy where the signals correspond to convolutions of electrons and holes at various energies within the VB and CB, here we directly map the time evolution of the hole energy distribution specifically in the VB. Taking advantage of the straightforward, one-particle interpretation of the N-edge core-level absorption, especially through the Te XUV edge, the intraband hole relaxation time scales are separated from the interband electron−hole recombination. The holes are found to redistribute within the VB on two distinct time scales of 15 ± 5 fs and 380 ± 90 fs. The former time constant is assigned to a thermalization process by carrier−carrier scattering, which leads to a shift in the peak of the hole energies closer toward the VB maximum. The slower hole redistribution time constant of 380 ± 90 fs is assigned to carrier−phonon cooling by intra- or intervalley scattering to the VB maximum, which is localized at the Γ critical point. These dynamics provide key insight regarding energy loss mechanisms following above-band-gap excitation of 2H-$MoTe_2$ thin films, which is important for designing next-generation photovoltaic or other optoelectronic devices using this layered semiconductor nanomaterial.

The present work furthermore reveals light-induced coherent lattice displacement dynamics along the out-of-plane A_{1g} and the in-plane E_{1g} phonon coordinates of 2H-$MoTe_2$. These structural dynamics show that the A_{1g} mode in particular is strongly coupled to the electronic excitation. The strong electron−phonon coupling in this out-of-plane mode leads to a new equilibrium structure in the excited state reached by expansion of the Te atoms away from the Mo plane. By extracting the real-space displacement of the 2H-$MoTe_2$ lattice following optical excitation, the measurements presented here provide a benchmark for understanding how structural changes in these materials are coupled to excited-state electronic structure. Our findings and experimental approach will be of benefit to the larger community that has a growing interest in light-induced lattice displacements in layered materials for applications toward optically controlled phase transitions.[13,15]

METHODS

Sample Preparation. The $MoTe_2$ thin film was synthesized by tellurizing a Mo film at 700 °C for 2 h in a tube furnace directly on a 30 nm thick, 3 × 3 mm^2 Si_3N_4 window. The Mo film was first deposited onto the Si_3N_4 window by sputtering previous to the reaction with Te powders. The as-synthesized $MoTe_2$ film was characterized by Raman spectroscopy and X-ray photoelectron spectroscopy (XPS). The Raman spectrum in the Supporting Information Figure S2 shows several modes including E_{1g}, A_{1g}, E_{2g}, indicating that the $MoTe_2$ film forms the 2H phase. Figure S3 in the Supporting Information shows the XPS spectrum of the 2H-$MoTe_2$ sample studied in this work. The relative peak spacing gives the spin−orbit splitting of the $4d_{5/2}$ and the $4d_{3/2}$ core levels of 1.5 eV. The detailed sample preparation and characterization can be found in the reference by Zhang et al.[3] Note that the synthesized $MoTe_2$ is a large area and continuous polycrystalline thin film.

Experimental Details. In the XUV transient absorption experiment, laser pulses centered at 790 nm with a pulse energy of 1.7 mJ and pulse duration of 30 fs from a Ti:sapphire amplifier (Femtopower Compact PRO) operating at 1 kHz repetition rate were focused into a hollow-core fiber filled with 1.5 bar of Ne to generate a supercontinuum spectrally spanning between 500 and 1000 nm. Dispersion compensation of the broad-band pulses was achieved through broad-band chirped mirrors (PC70, UltraFast Innovations) and a 2 mm thick ammonium dihydrogen phosphate crystal.[53] The laser beam was subsequently split into the probe and pump arm by a broad-band beam splitter with a 9:1 intensity ratio. A pair of fused silica wedges in each arm was used for fine-tuning of dispersion. With dispersion scan,[54] the pulse duration of the pump and the probe were characterized to be below 5 fs (Supporting Information Figure S1a). The laser beam in the probe arm was focused into a 4 mm long cell filled with Kr to generate broad-band XUV light (Supporting Information Figure S1c). The driving field in the probe arm was filtered by a 100 nm thick Al filter, and the XUV light subsequently focused into the sample chamber by a Au coated toroidal mirror in a 2f−2f geometry. The pump light was optically delayed and recombined with the probe by an annular mirror with a hole at 45 deg with respect to the mirror surface. To eliminate time delay drift, a transient absorption measurement on Ar $3s^3p^6$ np autoionizing states was run after each time-delay scan on the $MoTe_2$ sample.[21]

OCEAN and Density Functional Theory Calculations. Density functional theory (DFT) with the projector augmented wave (PAW) method[55] implemented in the Vienna *ab initio* Simulation Package (VASP)[56,57] was used to compute the ground-state density of states for bulk-$MoTe_2$ crystals. Exchange and correlation effects are calculated using the PBE form of GGA. Wave functions are constructed using a plane wave basis set with components up to a kinetic energy of 400 eV, and the reciprocal space is sampled using a 3 × 3 × 3 Gamma-centered mesh with a 0.05 eV Gaussian smearing of orbital occupancies. DFT simulations of lateral interfaces were performed on a bilayer $MoTe_2$ supercell containing 216 atoms, measuring 21.09 Å × 21.09 Å × 13.97 Å along the *a*-, *b*-, and *c*-directions. Calculations were performed until each self-consistency cycle is converged in energy to within 10^{-7} eV/atom and forces on ions are under 10^{-4} eV/Å.

The calculation of core-level absorption spectra at the Te $M_{4,5}$ edge was accomplished with DFT and Bethe−Salpeter equation (BSE) calculations using Quantum ESPRESSO and the OCEAN software package.[51,52,58,59] The DFT-BSE calculation was conducted using norm-conserving scalar-relativistic Perdew−Burke−Ernzerhof pseudopotentials with nonlinear core correction under generalized gradient approximation and a 6 × 6 × 1 k-point meshgrid.[60−63] In the calculation, the number of bands is set to 40 and the dielectric constant is set to 12.9. Convergence was achieved with an energy cutoff of 80 Ryd and cutoff radius of 4 Bohr.

https://dx.doi.org/10.1021/acsnano.0c06988
ACS Nano 2020, 14, 15829−15840

ASSOCIATED CONTENT

Supporting Information

The Supporting Information is available free of charge at https://pubs.acs.org/doi/10.1021/acsnano.0c06988.

Extended experimental methods, excited carrier density, sample preparation, density of states calculations, comparison of residual heat signal at 1 kHz and 100 Hz with the transient spectrum at 4−5 ps, Mo edge hole population dynamics, thermalized carriers−shift in peak maximum, comparison of monoexponential and biexponential fits to the time-dependent energy shift of the Te $4d_{5/2}$ → VB hole signal, decomposition of transient spectrum (0−10 fs), possible coherent phonon motion in the E^1_{2g} mode, and coherent phonon motion observed in "hole" signal and in Mo window. This manuscript has been previously submitted to a preprint server: A. R. Attar, H. Chang, A. Britz, X. Zhang, M. Lin, A. Krishnamoorthy, T. Linker, D. Fritz, D. M. Neumark, K. Rajiv, A. Nakano, P. Ajayan, P. Vashishta, U. Bergmann and S. R. Leone, Simultaneous Observation of Carrier-Specific Redistribution and Coherent Lattice Dynamics in 2H-$MoTe_2$ with Femtosecond Core-Level Spectroscopy, 2020, 2009.00721, arXiv.org. https://arxiv.org/abs/2009.00721 (Accessed October 13, 2020). (PDF)

AUTHOR INFORMATION

Corresponding Authors

Uwe Bergmann − *Stanford PULSE Institute, SLAC National Accelerator Laboratory, Menlo Park, California 94025, United States;* orcid.org/0000-0001-5639-166X; Email: bergmann@slac.stanford.edu

Stephen R. Leone − *Department of Chemistry and Department of Physics, University of California, Berkeley, California 94720, United States; Chemical Sciences Division, Lawrence Berkeley National Laboratory, Berkeley, California 94720, United States;* orcid.org/0000-0003-1819-1338; Email: srl@berkeley.edu

Authors

Andrew R. Attar − *Stanford PULSE Institute and Linac Coherent Light Source, SLAC National Accelerator Laboratory, Menlo Park, California 94025, United States;* orcid.org/0000-0002-9509-3857

Hung-Tzu Chang − *Department of Chemistry, University of California, Berkeley, California 94720, United States;* orcid.org/0000-0001-7378-8212

Alexander Britz − *Stanford PULSE Institute and Linac Coherent Light Source, SLAC National Accelerator Laboratory, Menlo Park, California 94025, United States;* orcid.org/0000-0002-1049-2841

Xiang Zhang − *Department of Materials Science and NanoEngineering, Rice University, Houston, Texas 77005, United States;* orcid.org/0000-0003-4004-5185

Ming-Fu Lin − *Linac Coherent Light Source, SLAC National Accelerator Laboratory, Menlo Park, California 94025, United States*

Aravind Krishnamoorthy − *Collaboratory for Advanced Computing and Simulations, University of Southern California, Los Angeles, California 90089, United States;* orcid.org/0000-0001-6778-2471

Thomas Linker − *Collaboratory for Advanced Computing and Simulations, University of Southern California, Los Angeles, California 90089, United States*

David Fritz − *Linac Coherent Light Source, SLAC National Accelerator Laboratory, Menlo Park, California 94025, United States*

Daniel M. Neumark − *Department of Chemistry, University of California, Berkeley, California 94720, United States; Chemical Sciences Division, Lawrence Berkeley National Laboratory, Berkeley, California 94720, United States;* orcid.org/0000-0002-3762-9473

Rajiv K. Kalia − *Collaboratory for Advanced Computing and Simulations, University of Southern California, Los Angeles, California 90089, United States*

Aiichiro Nakano − *Collaboratory for Advanced Computing and Simulations, University of Southern California, Los Angeles, California 90089, United States;* orcid.org/0000-0003-3228-3896

Pulickel Ajayan − *Department of Materials Science and NanoEngineering, Rice University, Houston, Texas 77005, United States;* orcid.org/0000-0001-8323-7860

Priya Vashishta − *Collaboratory for Advanced Computing and Simulations, University of Southern California, Los Angeles, California 90089, United States;* orcid.org/0000-0003-4683-429X

Complete contact information is available at: https://pubs.acs.org/10.1021/acsnano.0c06988

Author Contributions

A.R.A., H.-T.C., A.B., M.-F.L., U.B., D.F., S.R.L., P.V., and A.N. conceived of the experiments. X.Z. and P.A. synthesized and characterized the experimental samples. H.-T.C., A.R.A., and A.B. performed the experimental measurements and analyzed the results. H.-T.C., A.K., T.L., R.K., A.N., and P.V. performed the *ab initio* calculations. A.R.A., H.-T.C., U.B., and S.R.L. wrote the manuscript with discussion and input from all authors.

Author Contributions

▲A.R.A. and H.-T.C. contributed equally to this work

Notes

The authors declare no competing financial interest.

ACKNOWLEDGMENTS

This work was supported by the Computational Materials Sciences Program funded by the U.S. Department of Energy, Office of Science, Basic Energy Sciences, under Award No. DE-SC0014607. H.-T.C. and D.M.N. acknowledge support from the Air Force Office of Scientific Research (No. FA9550-14-1-0154). H.-T.C. is recently supported by the W. M. Keck Foundation Grant No. 046300. S.R.L. also acknowledges support by the U.S. Department of Energy, Office of Science, Office of Basic Energy Sciences, Materials Sciences and Engineering Division, under Contract No. DEAC02-05-CH11231, within the Physical Chemistry of Inorganic Nanostructures Program (KC3103) and support by Air Force Office of Scientific Research Grant FA9550-19-1-0314. The XUV transient absorption experiment is funded by the Air Force Office of Scientific Research (No. FA9550-14-1-0154) and the Army Research Office (No. W911NF-14-1- 0383). Core-level absorption simulations were conducted at the Molecular Graphics and Computation Facility, UC Berkeley, College of Chemistry, funded by the National Institute of

Health (NIH S10OD023532). Density functional theory simulations were performed at the Argonne Leadership Computing Facility under the DOE INCITE and Aurora Early Science programs and at the Center for High Performance Computing of the University of Southern California. We also thank Angel Garcia Esparza and John Vinson for their help with the OCEAN calculations and Romain Géneaux for the careful reading of this manuscript.

REFERENCES

(1) Manzeli, S.; Ovchinnikov, D.; Pasquier, D.; Yazyev, O. V.; Kis, A. 2D Transition Metal Dichalcogenides. *Nat. Rev. Mater.* **2017**, *2*, 1−15.
(2) Empante, T. A.; Zhou, Y.; Klee, V.; Nguyen, A. E.; Lu, I. H.; Valentin, M. D.; Naghibi Alvillar, S. A.; Preciado, E.; Berges, A. J.; Merida, C. S.; Gomez, M.; Bobek, S.; Isarraraz, M.; Reed, E. J.; Bartels, L. Chemical Vapor Deposition Growth of Few-Layer MoTe2 in the 2H, 1T′, and 1T Phases: Tunable Properties of MoTe2 Films. *ACS Nano* **2017**, *11*, 900−905.
(3) Zhang, X.; Jin, Z.; Wang, L.; Hachtel, J. A.; Villarreal, E.; Wang, Z.; Ha, T.; Nakanishi, Y.; Tiwary, C. S.; Lai, J.; Dong, L.; Yang, J.; Vajtai, R.; Ringe, E.; Idrobo, J. C.; Yakobson, B. I.; Lou, J.; Gambin, V.; Koltun, R.; Ajayan, P. M. Low Contact Barrier in 2H/1T′ MoTe2 in-Plane Heterostructure Synthesized by Chemical Vapor Deposition. *ACS Appl. Mater. Interfaces* **2019**, *11*, 12777−12785.
(4) Ruppert, C.; Aslan, O. B.; Heinz, T. F. Optical Properties and Band Gap of Single- and Few-Layer MoTe2 Crystals. *Nano Lett.* **2014**, *14*, 6231−6236.
(5) Choi, W.; Cho, M. Y.; Konar, A.; Lee, J. H.; Cha, G. B.; Hong, S. C.; Kim, S.; Kim, J.; Jena, D.; Joo, J.; Kim, S. High-Detectivity Multilayer MoS2 Phototransistors with Spectral Response from Ultraviolet to Infrared. *Adv. Mater.* **2012**, *24*, 5832−5836.
(6) Roy, T.; Tosun, M.; Kang, J. S.; Sachid, A. B.; Desai, S. B.; Hettick, M.; Hu, C. C.; Javey, A. Field-Effect Transistors Built from All Two-Dimensional Material Components. *ACS Nano* **2014**, *8*, 6259−6264.
(7) Duong, N. T.; Lee, J.; Bang, S.; Park, C.; Lim, S. C.; Jeong, M. S. Modulating the Functions of MoS2/MoTe2 van der Waals Heterostructure *via* Thickness Variation. *ACS Nano* **2019**, *13*, 4478−4485.
(8) Saenz, G. A.; Karapetrov, G.; Curtis, J.; Kaul, A. B. Ultra-High Photoresponsivity in Suspended Metal-Semiconductor-Metal Mesoscopic Multilayer MoS2 Broadband Detector from UV-to-IR with Low Schottky Barrier Contacts. *Sci. Rep.* **2018**, *8*, 1−11.
(9) Bertolazzi, S.; Krasnozhon, D.; Kis, A. Nonvolatile Memory Cells Based on MoS2/Graphene Heterostructures. *ACS Nano* **2013**, *7*, 3246−3252.
(10) Komsa, H. P.; Krasheninnikov, A. V. Electronic Structures and Optical Properties of Realistic Transition Metal Dichalcogenide Heterostructures from First Principles. *Phys. Rev. B: Condens. Matter Mater. Phys.* **2013**, *88*, 1−7.
(11) Yadav, D.; Trushin, M.; Pauly, F. Thermalization of Photoexcited Carriers in Two-Dimensional Transition Metal Dichalcogenides and Internal Quantum Efficiency of van der Waals Heterostructures. 2019, 1912.07480. arXiv.org. http://arxiv.org/abs/1912.07480 (Accessed October 12, 2020).
(12) Ji, H.; Lee, G.; Joo, M. K.; Yun, Y.; Yi, H.; Park, J. H.; Suh, D.; Lim, S. C. Thickness-Dependent Carrier Mobility of Ambipolar MoTe2: Interplay between Interface Trap and Coulomb Scattering. *Appl. Phys. Lett.* **2017**, *110*, 183501.
(13) Sie, E. J.; Nyby, C. M.; Pemmaraju, C. D.; Park, S. J.; Shen, X.; Yang, J.; Hoffmann, M. C.; Ofori-Okai, B. K.; Li, R.; Reid, A. H.; Weathersby, S.; Mannebach, E.; Finney, N.; Rhodes, D.; Chenet, D.; Antony, A.; Balicas, L.; Hone, J.; Devereaux, T. P.; Heinz, T. F.; Wang, X.; Lindenberg, A. M. An Ultrafast Symmetry Switch in a Weyl Semimetal. *Nature* **2019**, *565*, 61−66.
(14) Zhang, M. Y.; Wang, Z. X.; Li, Y. N.; Shi, L. Y.; Wu, D.; Lin, T.; Zhang, S. J.; Liu, Y. Q.; Liu, Q. M.; Wang, J.; Dong, T.; Wang, N. L. Light-Induced Subpicosecond Lattice Symmetry Switch in MoTe2. *Phys. Rev. X* **2019**, *9*, 1−9.
(15) Krishnamoorthy, A.; Bassman, L.; Kalia, R. K.; Nakano, A.; Shimojo, F.; Vashishta, P. Semiconductor-Metal Structural Phase Transformation in MoTe2Monolayers by Electronic Excitation. *Nanoscale* **2018**, *10*, 2742−2747.
(16) Li, L.; Lin, M. F.; Zhang, X.; Britz, A.; Krishnamoorthy, A.; Ma, R.; Kalia, R. K.; Nakano, A.; Vashishta, P.; Ajayan, P.; Hoffmann, M. C.; Fritz, D. M.; Bergmann, U.; Prezhdo, O. V. Phonon-Suppressed Auger Scattering of Charge Carriers in Defective Two-Dimensional Transition Metal Dichalcogenides. *Nano Lett.* **2019**, *19*, 6078−6086.
(17) Chi, Z.; Chen, H.; Zhao, Q.; Weng, Y. X. Ultrafast Carrier and Phonon Dynamics in Few-Layer 2H-MoTe2. *J. Chem. Phys.* **2019**, *151*, 114704.
(18) Krishnamoorthy, A.; Lin, M. F.; Zhang, X.; Weninger, C.; Ma, R.; Britz, A.; Tiwary, C. S.; Kochat, V.; Apte, A.; Yang, J.; Park, S.; Li, R.; Shen, X.; Wang, X.; Kalia, R.; Nakano, A.; Shimojo, F.; Fritz, D.; Bergmann, U.; Ajayan, P.; et al. Optical Control of Non-Equilibrium Phonon Dynamics. *Nano Lett.* **2019**, *19*, 4981−4989.
(19) Jhalani, V. A.; Zhou, J. J.; Bernardi, M. Ultrafast Hot Carrier Dynamics in GaN and Its Impact on the Efficiency Droop. *Nano Lett.* **2017**, *17*, 5012−5019.
(20) Pace, G.; Bargigia, I.; Noh, Y. Y.; Silva, C.; Caironi, M. Intrinsically Distinct Hole and Electron Transport in Conjugated Polymers Controlled by Intra and Intermolecular Interactions. *Nat. Commun.* **2019**, *10*, 1−11.
(21) Zürch, M.; Chang, H. T.; Borja, L. J.; Kraus, P. M.; Cushing, S. K.; Gandman, A.; Kaplan, C. J.; Oh, M. H.; Prell, J. S.; Prendergast, D.; Pemmaraju, C. D.; Neumark, D. M.; Leone, S. R. Direct and Simultaneous Observation of Ultrafast Electron and Hole Dynamics in Germanium. *Nat. Commun.* **2017**, *8*, 1−11.
(22) Zürch, M.; Chang, H. T.; Kraus, P. M.; Cushing, S. K.; Borja, L. J.; Gandman, A.; Kaplan, C. J.; Oh, M. H.; Prell, J. S.; Prendergast, D.; Pemmaraju, C. D.; Neumark, D. M.; Leone, S. R. Ultrafast Carrier Thermalization and Trapping in Silicon-Germanium Alloy Probed by Extreme Ultraviolet Transient Absorption Spectroscopy. *Struct. Dyn.* **2017**, *4*, 1−12.
(23) Lin, M. F.; Verkamp, M. A.; Leveillee, J.; Ryland, E. S.; Benke, K.; Zhang, K.; Weninger, C.; Shen, X.; Li, R.; Fritz, D.; Bergmann, U.; Wang, X.; Schleife, A.; Vura-Weis, J. Carrier-Specific Femtosecond XUV Transient Absorption of PbI2 Reveals Ultrafast Nonradiative Recombination. *J. Phys. Chem. C* **2017**, *121*, 27886−27893.
(24) Schultze, M.; Ramasesha, K.; Pemmaraju, C. D.; Sato, S. A.; Whitmore, D.; Gandman, A.; Prell, J. S.; Borja, L. J.; Prendergast, D.; Yabana, K.; Neumark, D. M.; Leone, S. R. Attosecond Bandgap Dynamics in Silicon. *Science* **2014**, *346*, 1348−1353.
(25) Schlaepfer, F.; Lucchini, M.; Sato, S. A.; Volkov, M.; Kasmi, L.; Hartmann, N.; Rubio, A.; Gallmann, L.; Keller, U. Attosecond Optical-Field-Enhanced Carrier Injection into the Gaas Conduction Band. *Nat. Phys.* **2018**, *14*, 560−564.
(26) Verkamp, M. A.; Leveillee, J.; Sharma, A.; Schleife, A.; Vura-Weis, J. *Bottleneck-Free Hot Hole Cooling in $CH_3NH_3PbI_3$ Revealed by Femtosecond XUV Absorption*. **2019**, 8323289. ChemRxiv.org. DOI: 10.26434/chemrxiv.8323289.v1 (Accessed October 12, 2020).
(27) Hamann-Borrero, J. E.; Macke, S.; Gray, B.; Kareev, M.; Schierle, E.; Partzsch, S.; Zwiebler, M.; Treske, U.; Koitzsch, A.; Büchner, B.; Freeland, J. W.; Chakhalian, J.; Geck, J. Site-Selective Spectroscopy with Depth Resolution Using Resonant X-Ray Reflectometry. *Sci. Rep.* **2017**, *7*, 1−11.
(28) Cushing, S. K.; Porter, I. J.; de Roulet, B. R.; Lee, A.; Marsh, B. M.; Szoke, S.; Vaida, M. E.; Leone, S. R. Layer-Resolved Ultrafast Extreme Ultraviolet Measurement of Hole Transport in a Ni-TiO2-Si Photoanode. *Sci. Adv.* **2020**, *6*, eaay6650.
(29) Hosler, E. R.; Leone, S. R. Characterization of Vibrational Wave Packets by Core-Level High-Harmonic Transient Absorption Spectroscopy. *Phys. Rev. A: At., Mol., Opt. Phys.* **2013**, *88*, 023420.
(30) Cushing, S. K.; Zürch, M.; Kraus, P. M.; Carneiro, L. M.; Lee, A.; Chang, H. T.; Kaplan, C. J.; Leone, S. R. Hot Phonon and Carrier

Relaxation in Si(100) Determined by Transient Extreme Ultraviolet Spectroscopy. *Struct. Dyn.* **2018**, *5*, 054302.
(31) Miller, N. A.; Deb, A.; Alonso-Mori, R.; Garabato, B. D.; Glownia, J. M.; Kiefer, L. M.; Koralek, J.; Sikorski, M.; Spears, K. G.; Wiley, T. E.; Zhu, D.; Kozlowski, P. M.; Kubarych, K. J.; Penner-Hahn, J. E.; Sension, R. J. Polarized XANES Monitors Femtosecond Structural Evolution of Photoexcited Vitamin B12. *J. Am. Chem. Soc.* **2017**, *139*, 1894−1899.
(32) Levantino, M.; Schirò, G.; Lemke, H. T.; Cottone, G.; Glownia, J. M.; Zhu, D.; Chollet, M.; Ihee, H.; Cupane, A.; Cammarata, M. Ultrafast Myoglobin Structural Dynamics Observed with an X-Ray Free-Electron Laser. *Nat. Commun.* **2015**, *6*, 6772.
(33) Cammarata, M.; Bertoni, R.; Lorenc, M.; Cailleau, H.; Di Matteo, S.; Mauriac, C.; Matar, S. F.; Lemke, H.; Chollet, M.; Ravy, S.; Laulhé, C.; Létard, J. F.; Collet, E. Sequential Activation of Molecular Breathing and Bending during Spin-Crossover Photoswitching Revealed by Femtosecond Optical and X-Ray Absorption Spectroscopy. *Phys. Rev. Lett.* **2014**, *113*, 1−5.
(34) Obara, Y.; Ito, H.; Ito, T.; Kurahashi, N.; Thürmer, S.; Tanaka, H.; Katayama, T.; Togashi, T.; Owada, S.; Yamamoto, Y. I.; Karashima, S.; Nishitani, J.; Yabashi, M.; Suzuki, T.; Misawa, K. Femtosecond Time-Resolved X-Ray Absorption Spectroscopy of Anatase TiO2 Nanoparticles Using XFEL. *Struct. Dyn.* **2017**, *4*, 044033.
(35) Shah, J. *Ultrafast Spectroscopy of Semiconductors and Semiconductor Nanostructures*; Springer-Verlag Berlin Heidelberg: New York, 1999.
(36) Richter, J. M.; Branchi, F.; Valduga De Almeida Camargo, F.; Zhao, B.; Friend, R. H.; Cerullo, G.; Deschler, F. Ultrafast Carrier Thermalization in Lead Iodide Perovskite Probed with Two-Dimensional Electronic Spectroscopy. *Nat. Commun.* **2017**, *8*, 1−7.
(37) Nie, Z.; Long, R.; Sun, L.; Huang, C. C.; Zhang, J.; Xiong, Q.; Hewak, D. W.; Shen, Z.; Prezhdo, O. V.; Loh, Z. H. Ultrafast Carrier Thermalization and Cooling Dynamics in Few-Layer MoS2. *ACS Nano* **2014**, *8*, 10931−10940.
(38) Rota, L.; Lugli, P.; Elsaesser, T.; Shah, J. Ultrafast Thermalization of Photoexcited Carriers in Polar Semiconductors. *Phys. Rev. B: Condens. Matter Mater. Phys.* **1993**, *47*, 4226−4237.
(39) Peng, B.; Zhang, H.; Chen, W.; Hou, B.; Qiu, Z. J.; Shao, H.; Zhu, H.; Monserrat, B.; Fu, D.; Weng, H.; Soukoulis, C. M. Sub-Picosecond Photo-Induced Displacive Phase Transition in Two-Dimensional MoTe2. *npj 2D Mater. Appl.* **2020**, *4*, 1−8.
(40) Rohde, G.; Stange, A.; Müller, A.; Behrendt, M.; Oloff, L. P.; Hanff, K.; Albert, T. J.; Hein, P.; Rossnagel, K.; Bauer, M. Ultrafast Formation of a Fermi−Dirac Distributed Electron Gas. *Phys. Rev. Lett.* **2018**, *121*, 256401.
(41) Bertoni, R.; Nicholson, C. W.; Waldecker, L.; Hübener, H.; Monney, C.; De Giovannini, U.; Puppin, M.; Hoesch, M.; Springate, E.; Chapman, R. T.; Cacho, C.; Wolf, M.; Rubio, A.; Ernstorfer, R. Generation and Evolution of Spin-, Valley-, and Layer-Polarized Excited Carriers in Inversion-Symmetric WSe2. *Phys. Rev. Lett.* **2016**, *117*, 1−5.
(42) Cushing, S. K.; Lee, A.; Porter, I. J.; Carneiro, L. M.; Chang, H. T.; Zürch, M.; Leone, S. R. Differentiating Photoexcited Carrier and Phonon Dynamics in the δ, L, and σ Valleys of Si(100) with Transient Extreme Ultraviolet Spectroscopy. *J. Phys. Chem. C* **2019**, *123*, 3343−3352.
(43) Froehlicher, G.; Lorchat, E.; Fernique, F.; Joshi, C.; Molina-Sánchez, A.; Wirtz, L.; Berciaud, S. Unified Description of the Optical Phonon Modes in N-Layer MoTe2. *Nano Lett.* **2015**, *15*, 6481−6489.
(44) Jeong, T. Y.; Jin, B. M.; Rhim, S. H.; Debbichi, L.; Park, J.; Jang, Y. D.; Lee, H. R.; Chae, D. H.; Lee, D.; Kim, Y. H.; Jung, S.; Yee, K. J. Coherent Lattice Vibrations in Mono- and Few-Layer WSe2. *ACS Nano* **2016**, *10*, 5560−5566.
(45) Trovatello, C.; Miranda, H. P. C.; Molina-Sánchez, A.; Borrego-Varillas, R.; Manzoni, C.; Moretti, L.; Ganzer, L.; Maiuri, M.; Wang, J.; Dumcenco, D.; Kis, A.; Wirtz, L.; Marini, A.; Soavi, G.; Ferrari, A. C.; Cerullo, G.; Sangalli, D.; Conte, S. D. Strongly Coupled Coherent Phonons in Single-Layer MoS2. *ACS Nano* **2020**, *14*, 5700−5710.
(46) Zeiger, H. J.; Vidal, J.; Cheng, T. K.; Ippen, E. P.; Dresselhaus, G.; Dresselhaus, M. S. Theory for Displacive Excitation of Coherent Phonons. *Phys. Rev. B: Condens. Matter Mater. Phys.* **1992**, *45*, 768−778.
(47) Dhar, L.; Rogers, J. A.; Nelson, K. A. Time-Resolved Vibrational Spectroscopy in the Impulsive Limit. *Chem. Rev.* **1994**, *94*, 157−193.
(48) Stevens, T. E.; Kuhl, J.; Merlin, R. Coherent Phonon Generation and the Two Stimulated Raman Tensors. *Phys. Rev. B: Condens. Matter Mater. Phys.* **2002**, *65*, 1−4.
(49) Riffe, D. M.; Sabbah, A. J. Coherent Excitation of the Optic Phonon in Si: Transiently Stimulated Raman Scattering with a Finite-Lifetime Electronic Excitation. *Phys. Rev. B: Condens. Matter Mater. Phys.* **2007**, *76*, 1−12.
(50) Melnikov, A. A.; Misochko, O. V.; Chekalin, S. V. Generation of Coherent Phonons in Bismuth by Ultrashort Laser Pulses in the Visible and NIR: Displacive *versus* Impulsive Excitation Mechanism. *Phys. Lett. A* **2011**, *375*, 2017−2022.
(51) Vinson, J.; Rehr, J. J.; Kas, J. J.; Shirley, E. L. Bethe-Salpeter Equation Calculations of Core Excitation Spectra. *Phys. Rev. B: Condens. Matter Mater. Phys.* **2011**, *83*, 115106.
(52) Gilmore, K.; Vinson, J.; Shirley, E. L.; Prendergast, D.; Pemmaraju, C. D.; Kas, J. J.; Vila, F. D.; Rehr, J. J. Efficient Implementation of Core-Excitation Bethe-Salpeter Equation Calculations. *Comput. Phys. Commun.* **2015**, *197*, 109−117.
(53) Timmers, H.; Sabbar, M.; Kobayashi, Y.; Neumark, D. M.; Leone, S. R. Polarization Assisted Amplitude Gating as a Route to Tunable, High-Contrast Single Attosecond Pulses. *Optica* **2016**, *3*, 707−710.
(54) Silva, F.; Miranda, M.; Alonso, B.; Rauschenberger, J.; Pervak, V.; Crespo, H. Simultaneous Compression, Characterization and Phase Stabilization of GW-Level 14 Cycle VIS-NIR Femtosecond Pulses Using a Single Dispersion-Scan Setup. *Opt. Express* **2014**, *22*, 10181.
(55) Blöchl, P. E. Projector Augmented-Wave Method. *Phys. Rev. B: Condens. Matter Mater. Phys.* **1994**, *50*, 17953−17979.
(56) Kresse, G.; Furthmüller, J. Efficient Iterative Schemes for *ab Initio* Total-Energy Calculations Using a Plane-Wave Basis Set. *Phys. Rev. B: Condens. Matter Mater. Phys.* **1996**, *54*, 11169−11186.
(57) Kresse, G.; Furthmüller, J. Efficiency of *ab Initio* Total Energy Calculations for Metals and Semiconductors Using a Plane-Wave Basis Set. *Comput. Mater. Sci.* **1996**, *6*, 15−50.
(58) Giannozzi, P.; Andreussi, O.; Bruume, T.; Enkovaara, J.; Rostgaard, C.; Mortensen, J. J. Advanced Capabilities for Materials Modelling with Quantum ESPRESSO. *J. Phys.: Condens. Matter* **2017**, *29*, 465901.
(59) Giannozzi, P.; Baroni, S.; Bonini, N.; Calandra, M.; Car, R.; Cavazzoni, C.; Ceresoli, D.; Chiarotti, G. L.; Cococcioni, M.; Dabo, I.; Dal Corso, A.; De Gironcoli, S.; Fabris, S.; Fratesi, G.; Gebauer, R.; Gerstmann, U.; Gougoussis, C.; Kokalj, A.; Lazzeri, M.; Martin-Samos, L.; et al. QUANTUM ESPRESSO: A Modular and Open-Source Software Project for Quantum Simulations of Materials. *J. Phys.: Condens. Matter* **2009**, *21*, 395502.
(60) Troullier, N.; Martins, J. L. Efficient Pseudopotentials for Plane-Wave Calculations. *Phys. Rev. B: Condens. Matter Mater. Phys.* **1991**, *43*, 1993−2006.
(61) Perdew, J. P.; Burke, K.; Ernzerhof, M. Generalized Gradient Approximation Made Simple. *Phys. Rev. Lett.* **1996**, *77*, 3865−3868.
(62) Louie, S.; Froyen, S.; Cohen, L. Nonlinear Ionic Pseudopotentials. *Phys. Rev. B: Condens. Matter Mater. Phys.* **1982**, *26* (4), 1738−1742.
(63) Grinberg, I.; Ramer, N. J.; Rappe, A. M. Transferable Relativistic Dirac-Slater Pseudopotentials. *Phys. Rev. B: Condens. Matter Mater. Phys.* **2000**, *62*, 2311−2314.

https://dx.doi.org/10.1021/acsnano.0c06988
ACS Nano 2020, 14, 15829−15840